# Fundamental Studies of Ruthenium Species Supported on Boron Nitride Nanotubes: Metal Loading and Pretreatment Effects on CO Oxidation

| | |
|---|---|
| Journal: | *Catalysis Science & Technology* |
| Manuscript ID | CY-ART-07-2024-000945.R1 |
| Article Type: | Paper |
| Date Submitted by the Author: | 13-Sep-2024 |
| Complete List of Authors: | Choi, Jinwon; Stony Brook University, Materials Science and Chemical Engineering<br>Pophali, Amol; Stony Brook University, Department of Materials Science Chemical Engineering<br>Kim, Byeongseok; Inha University, Chemistry and Chemical Engineering<br>Yoon, Kwangsuk; Hanyang University, Earth Resources and Environmental Engineering<br>Kim, Thomas You-Seok; NAiEEL Technology<br>Song, Hocheol; Hanyang University,<br>Shim, Sang Eun; Inha University, Chemical Engineering<br>Kim, Jaewoo; NAiEEL Technology<br>Kim, Tae Jin; Stony Brook University, Materials Science and Chemical Engineering |
| | |

1   **Fundamental Studies of Ruthenium Species Supported on Boron Nitride**

2   **Nanotubes: Metal Loading and Pretreatment Effects on CO Oxidation**

3   Jinwon Choi[a], Amol Pophali[a], Byeongseok Kim[b], Kwangsuk Yoon[c], Thomas You-Seok Kim[d],

4   Hocheol Song[c], Sang Eun Shim[b], Jaewoo Kim[d], Taejin Kim[*, a]

5   [a] Materials Science and Chemical Engineering Department, Stony Brook University,
6   StonyBrook, NY, 11794, U.S.A

7   [b] Department of Chemistry and Chemical Engineering, Education and Research Center for Smart
8   Energy and Materials, Inha University, Incheon, 22212, South Korea

9   [c] Department of Earth Resources and Environmental Engineering, Hanyang University, Seoul
10   04763, Republic of Korea

11   [d] R&D Center, NAiEEL Technology, Daejeon 34104, Republic of Korea

12

13

14

15

16

17   Corresponding Author: * TJK: Materials Science and Chemical Engineering Department, Stony
18   Brook University, Stony Brook, NY 11794, taejin.kim@stonybrook.edu

19

20

21 Abstract

22 Multiwalled boron nitride nanotube (BNNT), as a catalyst support, has become one of the promising
23 materials due to its high oxidation resistance and thermal stability. In this work, ruthenium (Ru) supported
24 on BNNT catalysts with different metal loading and treatment conditions was investigated for the CO
25 oxidation as a model reaction. To understand the physicochemical properties of prepared samples, a suite
26 of techniques, including FTIT, UV-Raman, SEM, TEM, and XPS, was utilized. The results showed that
27 the $RuO_x$ species were located on both the interior and exterior surfaces of BNNT, and an increase in
28 metal loading led to increased active sites. The 1 wt% $RuO_x$/BNNT (oxidized) exhibited better catalytic
29 activity than the 1 wt% Ru/BNNT (reduced), indicating that treatment conditions significantly affect the
30 catalytic properties. Reaction conditions, such as GHSV and the $O_2$/CO ratio, were varied to further
31 investigate the external mass transfer limitations and reaction mechanism of the 1 wt% $RuO_x$/BNNT
32 catalyst. The peculiar tubular morphology of BNNT resulted in negligible external mass transfer
33 limitation, and the catalyst might primarily follow the Eley-Rideal (ER) mechanism over the Langmuir-
34 Hinshelwood (LH) mechanism.

## 1. Introduction

35

36　　　　Boron nitride nanotube (BNNT) has attracted considerable attention as a promising

37　catalyst support due to its high oxidation resistance and superior thermal stability.[1–3] BNNT is

38　generally oxidized after 800 ℃, allowing BNNT to apply to high-temperature applications.[3,4]

39　High thermal stability can minimize the chronic problems of catalyst sintering and deactivation

40　caused by support collapse. In addition, these properties are one of the important keys for

41　hindering the nanoparticle sintering caused by particle migration and coalescence, and Ostwald

42　ripening mechanisms.[5,6] Recently, numerous theoretical studies reported that BNNT can be a

43　good candidate as a catalyst support due to its unique properties.[7–12] Q. Chen et al. designed

44　$Ru_B$@BNNT (doped a Ru atom into B vacancy in BNNT) using the density functional theory

45　(DFT) method and reported that the catalyst stability is superior to Ru@hexagonal boron nitride

46　nanosheet (h-BNNS).[13] The authors claimed that $Ru_B$@BNNT exhibits strong hybridization at

47　the Fermi level, leading to high structural stability. R. Chen et al. investigated the arsenic ($V$)

48　adsorption feasibility from water solutions over $Fe_3O_4$/BNNT and concluded that BNNT is a

49　promising supporting material due to its high oxidation resistance and physical stability.[14] Our

50　previous research also demonstrated that platinum group metals (PGMs) supported on the

51　functionalized BNNT (e.g., Pd/f-BNNT, Pt/f-BNNT, and Rh/f-BNNT) catalysts exhibited

52　outstanding catalytic activity and stability for NO reduction by CO oxidation due to the

53　synergetic effect of PGMs and BNNT.[15,16]

54　　　　Supported Ru catalysts have shown high catalytic activity in diverse fields, such as

55　ammonia decomposition,[17,18] water splitting,[19] $CO_2$ methanation,[20] CO oxidation,[21] etc. In the

56　past decades, researchers have tried to reduce Ru content in the catalyst due to its finite

57　resources, while achieving similar or better catalytic performance. It has been acknowledged that

58    the oxidation state of Ru species can significantly affect catalytic performance. K. Xu et al.

59    investigated the oxidation state effects of Ru species for CO oxidation using in-situ diffuse

60    reflectance infrared Fourier transform spectroscopy (in-situ DRIFTS).[22] The authors

61    demonstrated that $Ru^{n+}$ ($4 \leq n \leq 6$) are active species for the CO oxidation reaction, while $Ru^0$

62    are inactive species. J. Li et al. changed the oxidation state of Ru species supported on $CeO_2$

63    nanorod by varying oxidizing and reducing synthesis conditions.[23] The authors found that the

64    catalytic stability and performance on CO oxidation of the $5Ru/CeO_2$ NR-r with $Ru^{n+}$ ($4 \leq n \leq 6$)

65    species is better than that of the $5Ru/CeO_2$ NR-o with $Ru^{6+}$ species. W. Li et al. reported that the

66    catalytic performance on the CO oxidation of Ru/Graphene aerogels was decreased after

67    reduction treatment.[24] The authors concluded that the reduction treatment step (e.g., $Ru^{4+}$ to $Ru^0$)

68    made the inactive Ru species on graphene aerogel supports, which led to deactivation. These

69    results indicate that the oxidation state of Ru species plays a key role in the catalytic performance

70    for the CO oxidation reaction.

71        Based on the published papers, BNNT as catalyst support has a potential to improve

72    catalytic activity and stability. However, most existing research was conducted as theoretical

73    studies due to BNNT's supply shortages. Herein, we report an empirical study of $RuO_x/BNNT$

74    catalysts with different Ru loading and pretreatment steps (e.g., oxidizing and reducing). The

75    physical properties and morphology of synthesized catalysts were characterized by spectroscopic

76    and microscopic techniques. CO oxidation as a model chemical reaction over the synthesized

77    catalysts was studied to understand the effect of Ru loading and oxidation state on the catalytic

78    performance.

79

80    ## 2. Experimental section

81    **2.1 Catalyst synthesis**

82    Boron nitride nanotube (BNNT, purity >90 wt%, NAiEEL Technology) and ruthenium (III)

83    acetylacetonate ($Ru(C_5H_7O_2)_3$, Sigma-Aldrich) were used as a supporting material and a surface

84    species, respectively. The materials were used without further purification. For the synthesis of

85    $RuO_x$/BNNT catalysts, the following three steps were applied: (1) Predetermined Ru precursor

86    and BNNT were mixed using a mortar and pestle for 20 minutes, (2) The Ru precursor was

87    evaporated and interacted with the BNNT surface in an $N_2$ flow (UHP grade, total flow rate of 20

88    mL/min, 10 ℃/min) at 170 ℃ for 2 hrs and cooled down to room temperature, (3) The sample

89    was calcined in air (dry air, 20% oxygen and 80% nitrogen, total flow rate of 20 mL/min,

90    10 ℃/min) at 400 ℃ for 4 hrs. The oxidized samples were denoted as x wt% $RuO_x$/BNNT (x =

91    0.25, 0.5, and 1). In the case of 1 wt% Ru/BNNT catalyst, the 1 wt% $RuO_x$/BNNT was reduced

92    in a $H_2$ flow (10% $H_2$ balanced with $N_2$, total flow rate of 60 mL/min, 10 ℃/min) at 300 ℃ for 5

93    hrs. All samples were sieved (500 μm, Fieldmaster) to make uniform particle sizes.

94

95    **2.2 Characterization of catalysts**

96    To understand the molecular structures and bonding vibration of prepared samples, the Fourier

97    transform infrared (FTIR, Nicolet iS50, Thermo Scientific) and UV-Raman (325 nm, Renishaw

98    inVia confocal Raman microscope) were used. The UV-Raman spectra were collected in the

99    range of 1000-1800 cm$^{-1}$, and the acquisition time and the accumulation of the final spectrum

100   were 10 s and 30 scans, respectively. X-ray photoelectron spectroscopy (XPS) was used to

101   investigate the oxidation state of synthesized samples and obtained using monochromatic Al-Kα

102   radiation (hν = 1486.6 eV). The surface morphology of the catalysts was characterized by

103 scanning electron microscopy (SEM, EmCrafts cube 2, EmCrafts). Transmission electron

104 microscopy (TEM, JEM 2100F, JEOL)/EDS was performed to study the Ru species on the

105 BNNT surface. The Brunauer-Emmett-Teller (BET) and Barrett-Joyner-Halenda (BJH)

106 measurements were conducted to determine the specific surface area (SSA) and pore size

107 distribution (PSD), respectively, of the bulk BNNT using a Quantachrome NOVAtouch®

108 instrument. The tests were performed at -196 °C with $N_2$ (UHP grade) as adsorption-desorption

109 gas. Prior to measurement, the samples were degassed at 300 °C for 4 h under vacuum to remove

110 moisture and volatiles.

111

## 2.3 Catalytic Activity Tests

113 The catalytic performance on CO oxidation was evaluated in a fixed bed quartz reactor (OD 9.6

114 mm, ID 7 mm) connected with a mass flow controller (SLA5800 Series, Brooks Instrument).

115 The 40 mg of catalyst was loaded in the middle of the reactor and held in place by quartz wool

116 on each side. The sample was pretreated in a He flow (30 mL/min) at 400 °C for 30 min and then

117 cooled to room temperature. For the catalytic CO oxidation experiment, the composition of the

118 gas mixtures was 2 mL/min of CO, 20 mL/min of $O_2$, and 28 ml/min of He (Total flow rate: 50

119 mL/min and GHSV: 75 000 mL/$g_{catalyst}$/h). The reaction temperature was increased from room

120 temperature to 400 °C at a ramping rate of 1 °C/min. The composition of the product gas was

121 analyzed by online gas chromatography (TRACE™ 1300 GC, Thermo Scientific) equipped with

122 a thermal conductivity detector (TCD) and a capillary column (Carboxen 1010 PLOT). The CO

123 conversion was calculated using the following equation:

124 $$\text{CO conversion (\%)} = \frac{[CO]_{inlet} - [CO]_{outlet}}{[CO]_{inlet}} \times 100$$ where $[CO]_{inlet}$ and $[CO]_{outlet}$ represent the

125    influent and effluent CO concentrations at a certain temperature, respectively.

## 3. Results and Discussion

### 3.1 FTIR and UV-Raman Analysis

128    To understand the molecule structure of the samples, FTIR and UV-Raman spectroscopy were

129    performed. For comparison purposes, BNNT and Ru(acac)$_3$ samples' spectra were also obtained.

130    Fig. 1(a) shows the color changes of metal precursor, BNNT, and prepared samples (e.g.

131    Ru(acac)$_3$ (Red), BNNT (White), 1 wt% Ru(acac)$_3$/BNNT (Pink), 1 wt% Ru(acac)$_y$/BNNT

132    (Light pink), and 1 wt% RuO$_x$/BNNT (Grey)). As shown in Fig. 1(b), the spectra of BNNT, 1

133    wt% Ru(acac)$_3$/BNNT (after premixing step), 1 wt% Ru(acac)$_y$/BNNT (after evaporation step),

134    and 1 wt% RuO$_x$/BNNT (after calcination step) showed the same peaks at 762 and 1330 cm$^{-1}$,

135    which are corresponded to the B-N bending and B-N stretching modes, respectively.[15,16]

136    Compared to the BNNT, the 1 wt% Ru(acac)$_3$/BNNT displayed a distinct peak at 452 cm$^{-1}$,

137    which is assigned to an acetylacetonate vibration. Other Ru(acac)$_3$ related peaks between 500

138    and 1600 cm$^{-1}$ ranges, however, were not observed in 1 wt% Ru(acac)$_3$/BNNT spectra, due to the

139    overlap by the strong B-N bending and stretching peaks. In the case of 1 wt% Ru(acac)$_y$/BNNT

140    and 1 wt% RuO$_x$/BNNT, the peak at 452 cm$^{-1}$ disappeared, indicating that the metal ligands were

141    eliminated. However, the sample colors of 1 wt% Ru(acac)$_y$/BNNT (Light pink) and 1 wt%

142    RuO$_x$/BNNT (Grey) were different (Fig. 1(a)). This result indicates that the sample after the

143    evaporation step contains a small quantity of the acetylacetonate residues and it was fully

144    eliminated after the calcination step. As shown in Fig. 1(c), UV-Raman spectra of the BNNT and

145    three supported Ru samples (e.g., premixed, evaporated, and calcined) showed a peak at 1368

146    cm$^{-1}$, which corresponds to the E$_{2g}$ vibration mode of the BNNT.[25] Since the E$_{2g}$ peak was not

147    shifted, even after the calcination step, it is expected that BNNT has structural stability.
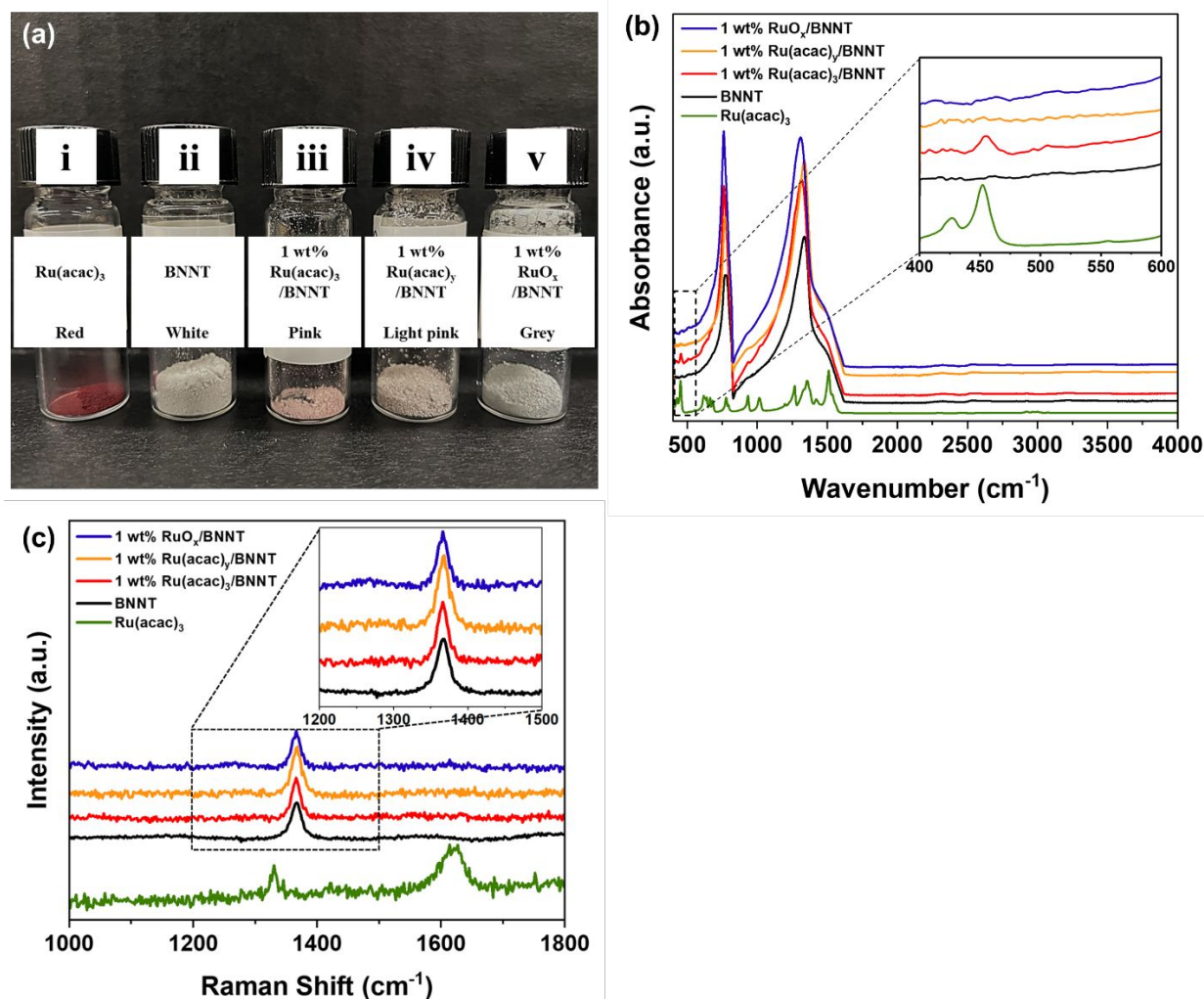
148

**Fig. 1** (a) a digital photo, (b) FTIR spectra, and (c) UV-Raman spectra of (i) Ru(acac)$_3$, (ii) as-
received BNNT, (iii) 1 wt% Ru(acac)$_3$/BNNT after premixing step, (iv) 1 wt% Ru(acac)$_y$/BNNT
after evaporation step, and (v) 1 wt% RuO$_x$/BNNT after calcination step.

152

### 3.2 SEM and TEM Analysis

The surface morphology of the 0.25, 0.5, 1 wt% RuO$_x$/BNNT, and 1 wt% Ru/BNNT was

investigated using SEM. All samples showed a 3-5 μm tube length as shown in Fig. 2. It is in

agreement with the bulk BNNT length studied by our previous research,[15] indicating that the

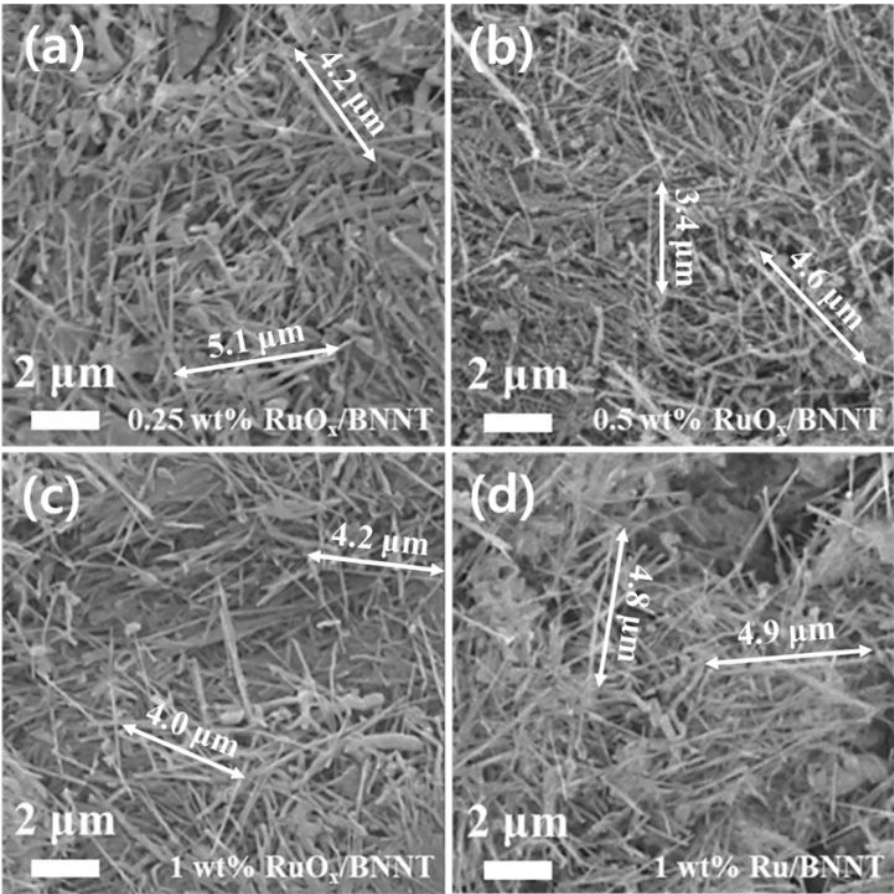catalyst synthesis processes did not affect the tube length and structure.

158

**Fig. 2** SEM images of (a) 0.25 wt% RuO$_x$/BNNT, (b) 0.5 wt% RuO$_x$/BNNT, (c) 1 wt%
RuO$_x$/BNNT, and (d) 1 wt% Ru/BNNT.

161

Fig. 3 shows the TEM results of 0.25, 0.5, 1 wt% RuO$_x$/BNNT, and 1 wt% Ru/BNNT. The inner

diameter of BNNT was 10-35 nm and the outer diameter of BNNT was 50-70 nm, which was

consistent with the pore size of the nanotube structure measured by BET (Fig. S1). According to

TEM images in low magnification (Fig. 3(a)-(d)), the presence of RuO$_x$ species increased with

increasing metal loading percentage, suggesting a corresponding augmentation of active sites on

the BNNT surface. As shown in Fig. 3(e)-(h), the Ru nanoparticles were observed on the outer

wall surface of BNNT. The particle sizes were 10-20 nm and some clusters were observed. It is

important to note that the nanoparticles were also consistently observed in the inner wall surface

170    of BNNT across all samples (Fig. 3(i)-(l)). In addition, these particles were found regardless of a

171    certain position in nanotubes, such as the edge and middle. Similar results have been reported by

172    D. Ugarte et al.[26] The authors synthesized carbon nanotubes (CNTs) filled with silver particles,

173    which was possible with tubes having an inner diameter of $\geq 4$ nm. The authors claimed that the

174    wide nanotube cavities (or thorough pores) are preferred for filling since the narrow cavities are

175    greatly affected by the van der Waals repulsion forces than the wide cavities, inhibiting metal

176    penetration into the tube cavities. X. Pan et al. reported that catalyst stability could be improved

177    by locating metal nanoparticles inside CNT due to the confinement effect.[27] The curvature of

178    CNT induces a shift in $\pi$-electron density from the interior surface to the external surface,

179    causing the internal metal nanoparticles to donate more electrons to the electron-deficient

180    internal surface. This results in stronger interactions between internal metal and internal surface

181    than the external metal and external surface, results in increasing catalyst stability. Z. Peralta-

182    Inga et al. computed the electrostatic potential on the inner and outer surfaces of BNNT and

183    reported that the potentials on the former are more positive than on the latter (i.e., the curvature

184    of BNNT induces the $\pi$-electron density to be shifted towards the external surface than the

185    interior surface).[28] Thus, metal nanoparticles inside the internal surface of BNNT would also be

186    strongly confined. In the present work, the wide nanotube cavities of BNNT (inner diameater:10-

187    35 nm) would allow the Ru nanoparticles to be formed inside the inner surface of BNNT, leading

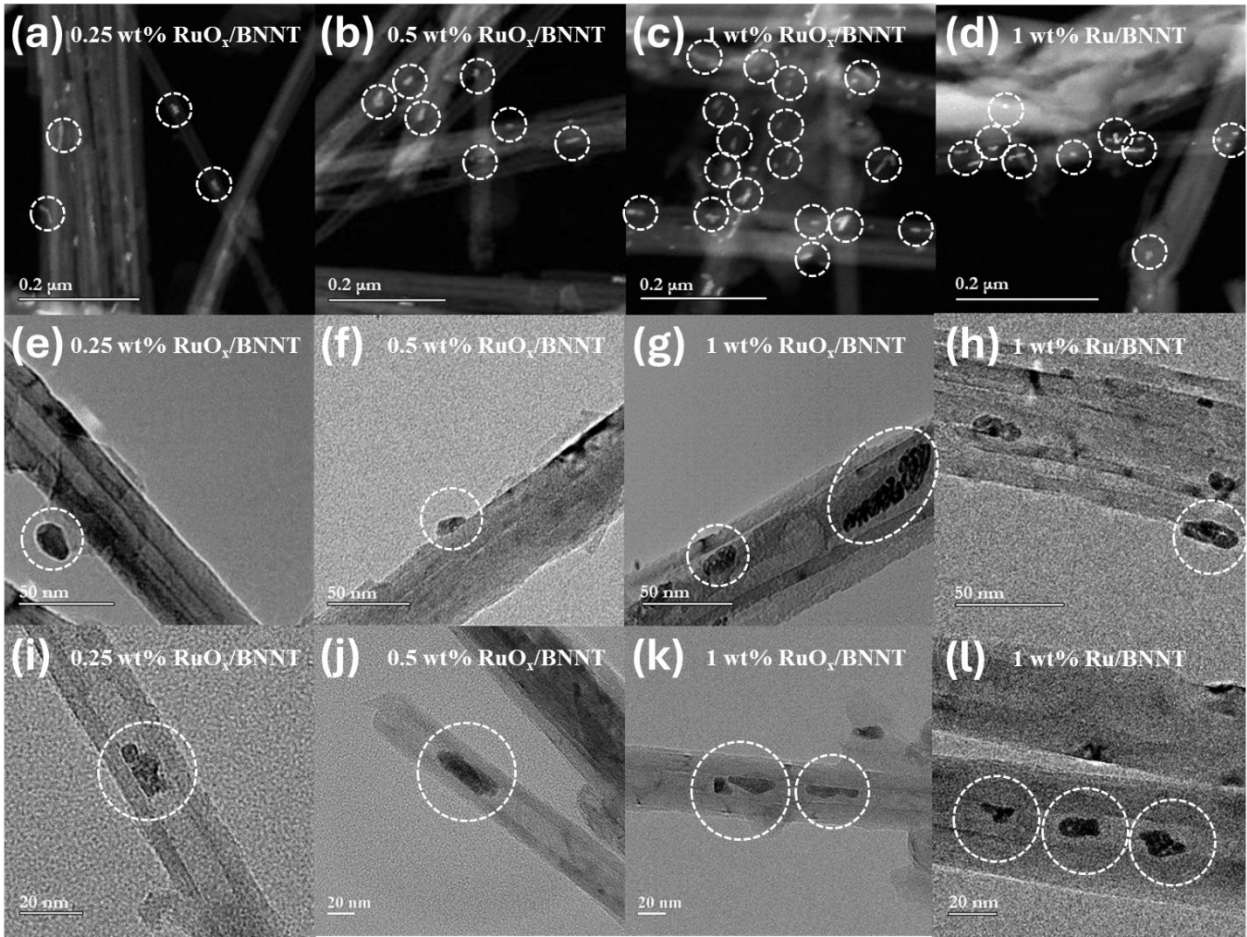188    to the confinement effect.

189

**Fig. 3** TEM images of 0.25, 0.5, 1 wt% $RuO_x$/BNNT and 1 wt% Ru/BNNT: (a-d) low magnification, (e-h) Ru species on outer wall BNNT, and (i-l) Ru species on inner wall BNNT. Dotted circle: $RuO_x$ or Ru particles.

193

194  To further explore the shape and location of $RuO_x$ particles inside BNNT, pristine BNNT and 1

195  wt% $RuO_x$/BNNT were investigated. Fig. 4(a) shows the TEM results of pristine BNNT, where

196  regular dark spots and an independent BNNT (red arrow) inside another BNNT were observed.

197  Based on the previous study by A. Celik-Aktas et al., these dark spots indicate high crystallinity,

198  which is characteristic of BNNT synthesized with a double-helix structure.[29] It is worthwhile to

199  note that $RuO_x$ particle sizes (e.g., 15.1 nm and 32.5 nm) and shapes (e.g., oval and circle) were

200  varied with different inner diameter of BNNT (Fig. 4(b)). The individual BNNT can disturb the

201    migration of partial Ru precursors during catalyst synthesis, leading to the growth of particles in

202    locations with different inner diameters. If the $RuO_x$ species had grown on the outer wall surface

203    of BNNT, the particle sizes would not match the inner wall line (Fig. 3(g)).
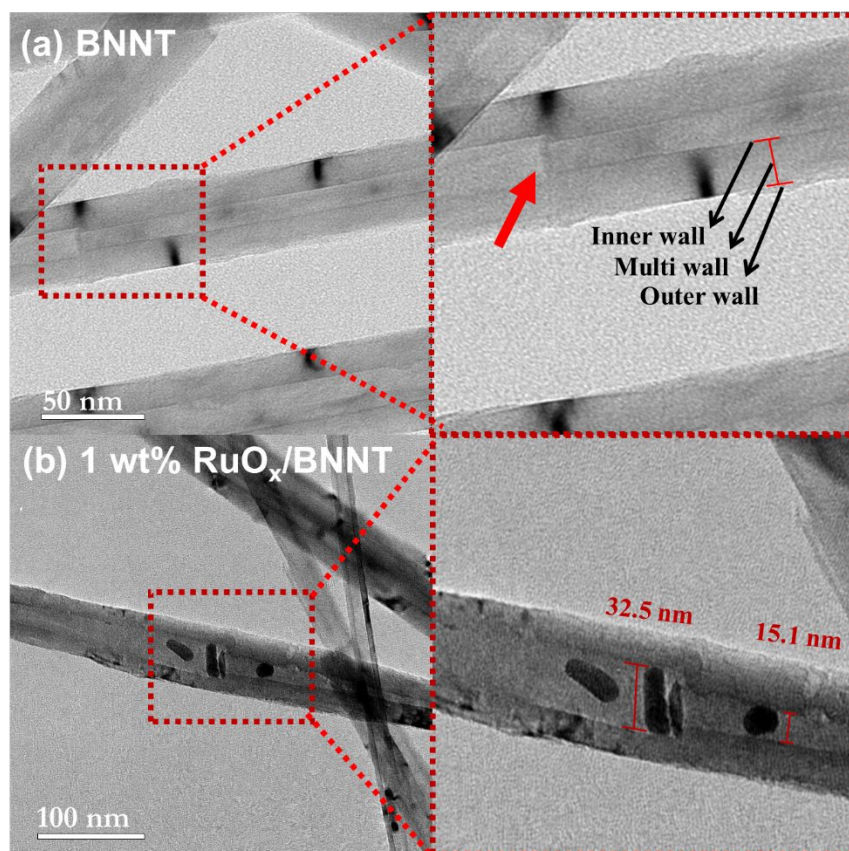


204

205    **Fig. 4** TEM images of (a) BNNT and (b) 1 wt% $RuO_x$/BNNT.

206

### 3.3 XPS Analysis

208    In order to analyze the oxidation state of Ru species in the 1 wt% $RuO_x$/BNNT and 1 wt%

209    Ru/BNNT catalysts, XPS characterization was performed. Fig. 5 demonstrates the XPS spectra

210    of the Ru 3d energy regions. The variation of peak intensity was observed, especially at $\leq 283.5$

211    eV. Three different Ru $3d_{5/2}$ peaks at around 280.8, 281.6, and 283.1 eV can be assigned to $Ru^{4+}$,

212    $Ru^{n+}$ ($4 \leq n \leq 6$), and $Ru^{6+}$, respectively.[30,31] S.L. Rodriguez et al. studied the oxidation state of

213    Ru of the series of $RuO_x/CeO_2$ catalysts by combining TPR, XRD, and XPS.[32] Although the

214    authors did not fully distinguish the oxidation state of the Ru, the authors assigned the $Ru3d_{5/2}$

215    regions containing $Ru^{4+}$ and cationic species of Ru (or $Ru^{n+}$) in the $CeO_2$ lattice. K. Qadir et al.,

216    reported in-situ XPS for Ru nanoparticles under oxidation and reduction conditions.[33] The

217    authors provided the reversibility of Ru between $Ru^0$ (279.8 eV) and $Ru^{4+}$ (280.7 eV). It should

218    be noted that the analysis of $Ru3d_{3/2}$ regions at > 284 eV was more complicated since C1s peak

219    (~285.0 eV) is overlapped with Ru peaks. Based on the literature review, it is concluded that 1

220    wt% $RuO_x/BNNT$ (oxidation treatment) sample contains $Ru^{n+}$ species dominantly, while 1 wt%

221    Ru/BNNT (reduction treatment) sample contains $Ru^{4+}$ species dominantly. The XPS results

222    provide that the oxidation state of Ru species supported on BNNT depends on treatment

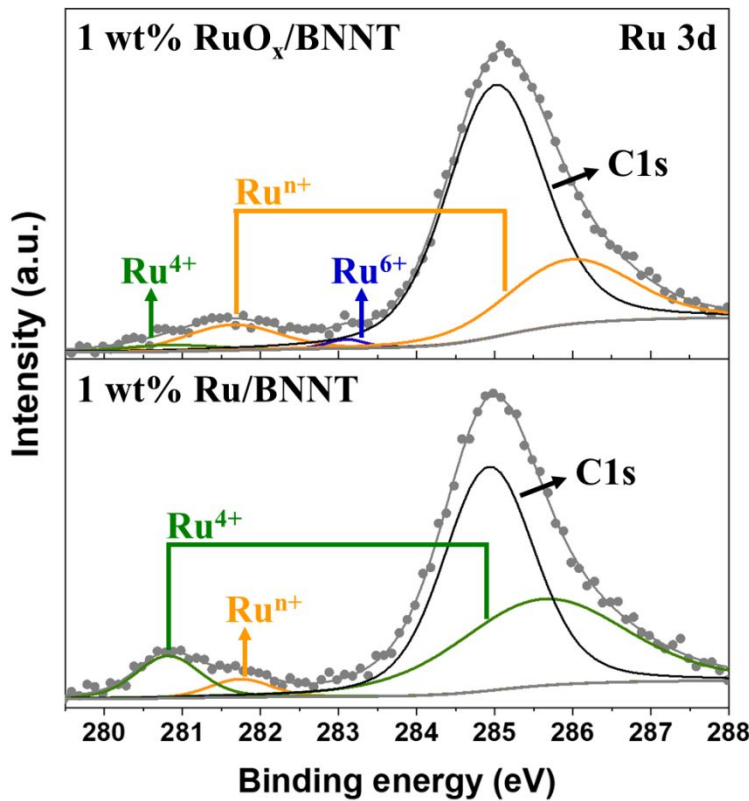223    conditions, which may influence the catalytic properties.



224

225  **Fig. 5** XPS spectra of Ru 3d for 1 wt% $RuO_x$/BNNT and 1 wt% Ru/BNNT. The Shirley-type
226  background was applied.

227

228  **3.4 Catalytic CO Oxidation Performance**

229  Fig. 6(a) and Table 1 show the catalytic performance of the series of $RuO_x$/BNNT samples as

230  well as the bulk BNNT. CO oxidation would occur simultaneously at the active sites on the

231  exterior and interior surface since BNNT provides enough space to penetrate the carbon

232  monoxide (kinetic diameter: 3.76 Å) and oxygen molecules (kinetic diameter:3.46 Å).[34] The

233  temperature at 50% CO conversion ($T_{50}$) was decreased with increasing of $RuO_x$ loadings: 1 wt%

234  $RuO_x$/BNNT (208 ℃) < 0.5 wt% $RuO_x$/BNNT (216 ℃) < 0.25 wt% $RuO_x$/BNNT (240 ℃) at

235  GHSV 75,000 mL/$g_{catalyst}$/h. It is worth noticing that the bulk BNNT did not show any catalytic

236  activity, indicating that $RuO_x$ species on the BNNT surface are active sites for CO oxidation. It

237  agrees with the previous report studied by I. Rossetti et al.[35] The authors investigated the effect

238  of Ru loading on ammonia synthesis and claimed that increasing Ru content from 1.9 wt% to 3.8

239  wt% led to an increase in active sites. The reported results for CO oxidation using supported Ru

240  catalysts are summarized in Table 2.

241  The effect of oxidizing and reducing treatment was investigated (Fig. 6(b)). The $T_{10}$, $T_{50}$, and $T_{90}$

242  of 1 wt% $RuO_x$/BNNT were 194, 208, and 218 ℃ and those of 1wt% Ru/BNNT were 230, 246,

243  and 262 ℃, respectively. This result provides that the catalytic property for the CO oxidation is

244  directly related to the oxidation state of Ru. XPS results (Fig. 5) show that the 1 wt%

245  $RuO_x$/BNNT has mainly $Ru^{n+}$ species, while the 1 wt% Ru/BNNT has primarily $Ru^{4+}$ species. J.

246  Li et al. investigated the effect of metal oxidation state using Ru supported on $CeO_2$ and

247  demonstrated that the $Ru^{n+}$ rich surface is more favorable for the catalytic CO oxidation than

248  $Ru^{4+}$ or $Ru^{6+}$ rich surface.[23] K. Xu et al. studied the Ru active species using DRIFTS and

249    reported that the CO adsorbed on $Ru^{n+}$ species are more rapidly converted to $CO_2$ gases than that

250    on $Ru^0$ species at the same temperature.[22] Thus, the predominant $Ru^{n+}$ species in the 1 wt%

251    $RuO_x$/BNNT would improve the catalytic performance as active species.

252    The effect of the mass transfer limitation on the CO oxidation of 1 wt% $RuO_x$/BNNT was

253    investigated by changing the GHSV conditions from 37,500 to 150,000 mL/$g_{catalyst}$/h. As shown

254    in Fig 6(c), CO catalytic performance was very similar (or slightly changed) with increasing

255    GHSV conditions, indicating that the 1 wt% $RuO_x$/BNNT is not affected by the external mass

256    transfer limitation. This result originates from the peculiar tubular morphology of nanotubes,

257    specifically the absence of micropores. This is further confirmed from Fig. S1 showing the BET

258    and PSD data. In the case of the conventional porous supported catalysts, a low external to

259    internal surface area ratio is expected. Consequently, it leads to difficulties in diffusion and

260    accessibility of reactants to active sites. In addition, products hinder the diffusion of reactants by

261    escaping to the same path of the blind pore, thereby contributing to the formation of stagnant

262    film.[36] On the other hand, the nanotube structure contains cavities (or thorough pores) and a high

263    external to internal surface area ratio, facilitating easy diffusion and accessibility of reactants to

264    active sites. Moreover, products do not impede the diffusion of reactants by escaping through the

265    other exit, thereby resulting in the formation of negligible stagnant film. The SSA from the BET

266    analysis was calculated to be ~48.50 $m^2$/g, and the isotherm (Fig. S1 (a)) confirms meso-

267    macroporous configuration. The PSD and cumulative pore volume data (Fig. S1 (b)) reveal a

268    mesoporous range of ~10–30 nm with minor $N_2$ adsorption, while the majority of adsorption

269    occurred on the external surface of the BNNT. This data supports the hypothesis of negligible

270    mass transfer limitation over $RuO_x$/BNNT catalysts during the CO oxidation reaction. CNT-

271    based catalysts have consistently reported similar results, although experimental demonstration is

272    still debatable.[37–39]

273    The Eley-Rideal (ER) and the Langmuir-Hinshelwood (LH) mechanisms have been proposed to

274    understand the CO oxidation reaction over the supported metal oxide catalysts.[40–42] Fig. 7 shows

275    the proposed ER and RH mechanisms. The ER mechanism occurs in the interaction between a

276    CO gas molecule and an adsorbed O atom on the active site. Initially, an $O_2$ is adsorbed and

277    dissociates into the two O atoms ($O_2(g) + 2^* \leftrightarrow 2O^*$) on the active site. Then, a CO molecule

278    approaches the active site and reacts with the adsorbed O atom to form a $CO_2$ molecule ($CO(g) +$

279    $O^* \leftrightarrow CO_2(g) + ^*$). In the case of the LH mechanism, the reaction occurs through the interaction

280    between an adsorbed CO molecule and an adsorbed O atom on the active site. Both CO and $O_2$

281    molecules are respectively adsorbed on the active site ($O_2(g) + 2^* \leftrightarrow 2O^*$ and $CO(g) + ^* \leftrightarrow$

282    $CO^*$). Then an adsorbed CO molecule reacts with a vicinal adsorbed O atom to form a $CO_2$

283    molecule ($CO^* + O^* \leftrightarrow CO_2(g) + 2^*$). The reaction mechanism of the CO oxidation over 1 wt%

284    $RuO_x$/BNNT was investigated by varying the CO to $O_2$ ratio from 1:1 to 1:10. As shown in Fig.

285    6(d), the CO conversion was improved with increasing $O_2$ ratio from 1:1 to 1:5 ratio: $T_{50} =$

286    205 ℃ (1:5) < 231 ℃ (1:2.5) < 244 ℃ (1:1). Further increased $O_2$/CO ratio, however, did not

287    affect the catalytic activity. C. Peden et al. studied the CO oxidation mechanism on Ru (001)

288    surface using DRIFTS with varied $O_2$/CO ratios.[43] Since the chemisorbed CO peak was

289    gradually decreased with increasing oxygen pressure, the authors claimed that the Ru (001)

290    surface follows the ER mechanism under oxidizing conditions over the LH mechanism. It was

291    also reported that the $CO_2$ formation rate increases with the oxygen pressure up to 2.5 Torr,

292    beyond which it remains constant regardless of oxygen pressure. C. Huang et al. investigated the

293    CO oxidation of Ru/hBN catalyst using the periodic DFT method.[44] The authors reported that the

294    $O_2$ molecules will be primarily adsorbed on the Ru atoms over CO molecules since the

295    adsorption energy of $O_2$ (-2.43 eV) is lower than that of CO (-1.95 eV). Based on the literature

296    review and obtained activity results, it is concluded that the 1 wt% $RuO_x$/BNNT catalyst is

297    favorable for the ER mechanism over the LH mechanism (Fig. 7).
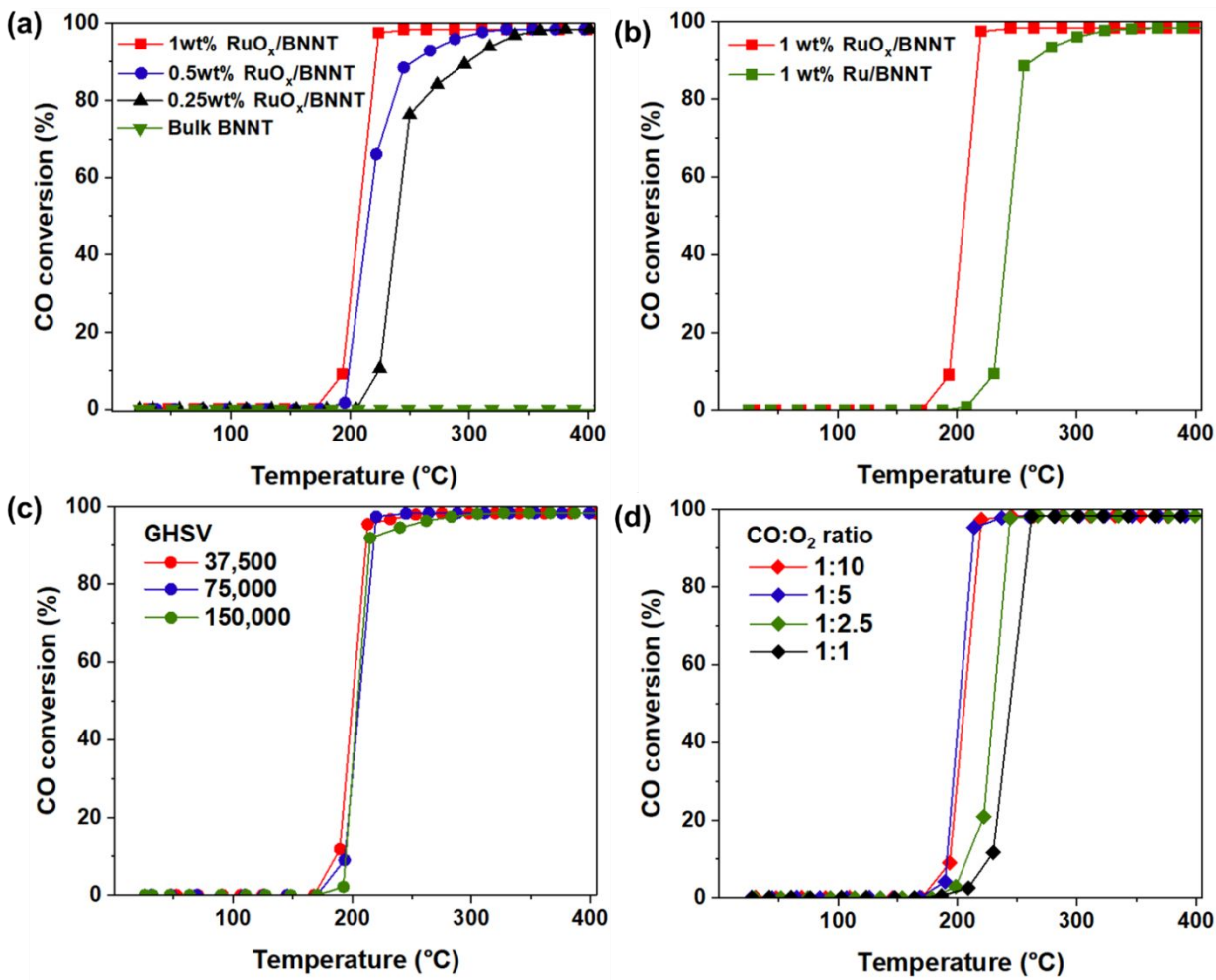


298

299    **Fig. 6** CO conversion as a function of reaction temperature. (a) Ru loading effect, (b) treatment
300    condition effect, (c) GHSV effect using 1 wt% $RuO_x$/BNNT, and (d) CO to $O_2$ ratio effect using
301    1 wt% $RuO_x$/BNNT. Reaction conditions: (a, b) GHSV = 75,000 (mL/$g_{catalyst}$/h), CO:$O_2$ ratio =
302    1:10, (c) CO:$O_2$ ratio = 1:10, (d) GHSV = 75,000 (mL/$g_{catalyst}$/h).

303

304    **Table 1** The CO conversion results of $RuO_x$/BNNT catalysts with different Ru loading,
305    treatment steps, and experimental conditions

| Catalysts | CO:$O_2$ Gas Ratio | GHSV (mL $g_{cat}^{-1}$ $h^{-1}$) | $T_{10}$ (°C) | $T_{50}$ (°C) | $T_{90}$ (°C) |
|---|---|---|---|---|---|
| **Loading and treatment condition effects** | | | | | |
| Bulk BNNT | 1:10 | 75,000 | - | - | - |
| 0.25 wt% RuO$_x$/BNNT | 1:10 | 75,000 | 224 | 240 | 300 |
| 0.5 wt% RuO$_x$/BNNT | 1:10 | 75,000 | 200 | 216 | 253 |
| 1 wt% RuO$_x$/BNNT | 1:10 | 75,000 | 194 | 208 | 218 |
| 1 wt% Ru/BNNT | 1:10 | 75,000 | 230 | 246 | 262 |
| **GHSV effect** | | | | | |
| 1 wt% RuO$_x$/BNNT | 1:10 | 37,500 | 191 | 200 | 210 |
| 1 wt% RuO$_x$/BNNT | 1:10 | 75,000 | 194 | 208 | 218 |
| 1 wt% RuO$_x$/BNNT | 1:10 | 150,000 | 194 | 208 | 215 |
| **CO:$O_2$ ratio effect** | | | | | |
| 1 wt% RuO$_x$/BNNT | 1:10 | 75,000 | 194 | 208 | 218 |
| 1 wt% RuO$_x$/BNNT | 1:5 | 75,000 | 192 | 205 | 214 |
| 1 wt% RuO$_x$/BNNT | 1:2.5 | 75,000 | 209 | 231 | 241 |
| 1 wt% RuO$_x$/BNNT | 1:1 | 75,000 | 226 | 244 | 260 |
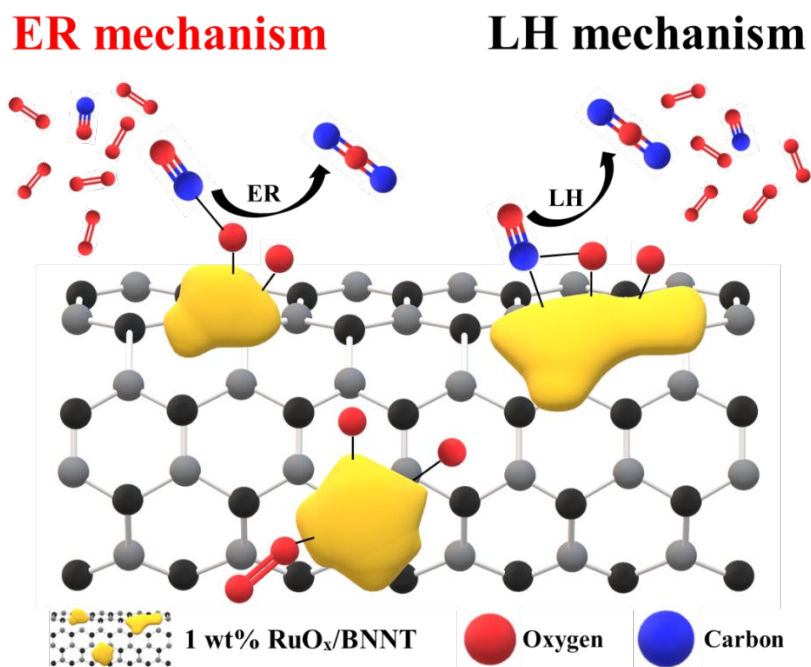


**Fig 7.** Schematic illustration of the proposed reaction mechanism for CO oxidation on 1 wt% RuO$_x$/BNNT catalyst.

311    **Table 2** Catalytic performance comparison with previously reported catalysts for CO Oxidation

| Catalysts | Ru loading (wt %) | Treatment step | CO conc. (Vol %) | $CO:O_2$ Gas Ratio | GHSV (mL $g_{cat}^{-1}$ $h^{-1}$) | $T_{10}$ (°C) | $T_{50}$ (°C) | $T_{90}$ (°C) | Ref. |
|---|---|---|---|---|---|---|---|---|---|
| $Ru/CeO_2NR$-r | 5.0 | Reduction | 1 | 1:20 | 36,000 | 25 | 50 | 102 | 23 |
| $Ru/Al_2O_3$ | 2.0 | - | 1.564 | 1:2 | 25,200 | 120 | 134 | 180 | 45 |
| $Ru/C12A7:e^-$ | 2.0 | - | 1.564 | 1:2 | 25,200 | 87 | 125 | 134 | 45 |
| $Ru_{(1.5)}CeO_2$ | 1.5 | Reduction | 1 | 1:0.5 | Contact time $W/F_{CO}$ = 7.4 $g_{cat}$ h $mol_{CO}^{-1}$ | 50 | 90 | 140 | 46 |
| Ru NWs/$TiO_2$ | 1.2 | - | 1 | 1:1 | 12,600 | 84 | 126 | 143 | 47 |
| fcc-Ru NPs/ $\gamma$-$Al_2O_3$ | 1.0 | Reduction | 1 | 1:1 | 20,000 | 115 | 141 | 160 | 48 |
| $Ru/TiO_2$ | 1.0 | Oxidation | 3500 ppm | - | 60,000 | 78 | 120 | 128 | 49 |
| $Ru/CeO_2NR$-r | 1.0 | Reduction | 1 | 1:20 | 36,000 | 47 | 78 | 105 | 50 |
| $Ru/SiO_2$-r | 1.0 | Reduction | 1 | 1:20 | 36,000 | 236 | 297 | 370 | 50 |
| $RuO_x/BNNT$ | 1.0 | Oxidation | 4 | 1:10 | 150,000 | 194 | 208 | 215 | This work |

312

313

## 4. Conclusions

315    In this study, $RuO_x/BNNT$ catalysts with different Ru loading and pretreatment steps were
316    synthesized and applied to CO oxidation as a model reaction. TEM results confirmed that the Ru
317    nanoparticles with 10-20 nm were introduced to both the internal and external surfaces of
318    BNNT. The CO conversion results improved with increasing Ru loading and the oxidized
319    catalyst exhibited higher activity than the reduced sample. The XPS revealed that $Ru^{n+}$ species
320    shifted to $Ru^{4+}$ species after reduction treatment, suggesting that $Ru^{n+}$ plays a critical role in
321    enhancing catalytic activity. The 1 wt% $RuO_x/BNNT$ catalyst was further investigated by
322    changing the reaction conditions (e.g., GHSV and $O_2/CO$ ratio). The GHSV conditions did not
323    affect the activity, suggesting no external mass transfer limitation on the catalyst. The absence of
324    micropores in the nanotube made a high ratio of external to internal surface area compared to the
325    conventional porous materials, resulting in easy accessibility of reactants to metal active sites
326    without external diffusion limitation. In addition, both open ends of the nanotube can minimize
327    the diffusion competition between the reactants and products, contributing to the formation of
328    negligible stagnant film. The catalyst will be favorable to the ER mechanism over the LH
329    mechanism, as the catalytic performance was increased with increasing CO to $O_2$ ratio from 1:1
330    to 1:5.

331

## Author Contributions

333    J. Choi: Methodology, Formal analysis, Writing – original draft, Writing – review & editing, A.
334    Pophali: Formal analysis, Writing – review & editing, B. Kim: Formal analysis, K. Yoon:
335    Formal analysis, H. Song: Formal analysis, S. Shim: Formal analysis, J. Kim: Formal analysis, T.
336    Kim: Supervision, Writing – review & editing, Project administration, Funding acquisition. All
337    authors have given approval to the final version of the manuscript.

338

## Conflicts of interest

340   There are no conflicts of interest to declare.

341

348

## References

350   1  D. Golberg, Y. Bando, C. C. Tang and C. Y. Zhi, *Adv. Mater.*, 2007, **19**, 2413–2432.
351   2  D. Golberg, Y. Bando, Y. Huang, T. Terao, M. Mitome, C. Tang and C. Zhi, *ACS Nano*, 2010,
352      **4**, 2979–2993.
353   3  J.-W. Seo, A. Pophali, S. An, C. S. L. Liang, S. Li, H. Liu, J. Kim, K. An, J. Kim and T. Kim,
354      *J. Mol. Struct.*, 2025, **1319**, 139545.
355   4  Y. Chen, J. Zou, S. J. Campbell and G. Le Caer, *Appl. Phys. Lett.*, 2004, **84**, 2430–2432.
356   5  T. W. Hansen, A. T. DeLaRiva, S. R. Challa and A. K. Datye, *Acc. Chem. Res.*, 2013, **46**,
357      1720–1730.
358   6  H. Xiong, A. K. Datye and Y. Wang, *Adv. Mater.*, 2021, **33**, 2004319.
359   7  S. Lin, X. Ye and J. Huang, *Phys. Chem. Chem. Phys.*, 2015, **17**, 888–895.
360   8  S. Abdel Aal, *Surf. Sci.*, 2016, **644**, 1–12.
361   9  H. Xu, K. Ni, X. Li, S. Zhu and G. Fan, *Comput. Theor. Chem.*, 2017, **1115**, 37–44.
362   10 Y. Zhang, Y. Liu, Z. Meng, C. Ning, C. Xiao, K. Deng, P. Jena and R. Lu, *Phys. Chem.*
363      *Chem. Phys.*, 2018, **20**, 17599–17605.
364   11 N. H. Jabarullah, R. Razavi, Mohadeseh Yazdani Hamid, Qahtan. A. Yousif and M. Najafi,
365      *Prot. Met. Phys. Chem. Surf.*, 2019, **55**, 671–676.
366   12 T. Yang, X.-Q. Han, H.-L. Xu and Z.-M. Su, *Appl. Surf. Sci.*, 2021, **549**, 149314.
367   13 Q. Chen, Q. Ke, X. Zhao and X. Chen, *Diam. Relat. Mater.*, 2023, **136**, 109942.
368   14 R. Chen, C. Zhi, H. Yang, Y. Bando, Z. Zhang, N. Sugiur and D. Golberg, *J. Colloid Interface*
369      *Sci.*, 2011, **359**, 261–268.
370   15 K.-I. Choi, D. Yadav, J. Jung, E. Park, K.-M. Lee, T. Kim and J. Kim, *ACS Appl. Mater.*
371      *Interfaces*, 2023, **15**, 10670–10678.
372   16 J. K. Kim, C. Jin, J. Park, M. Iloska, M. Kim, D. Seo, J. Jung, T. Kim and J. Kim, *Ind. Eng.*
373      *Chem. Res.*, 2019, **58**, 20154–20161.
374   17 S. Kang, J. Cha, Y. S. Jo, Y. Lee, H. Sohn, Y. Kim, C. K. Song, Y. Kim, D. Lim, J. Park and
375      C. W. Yoon, *Adv. Mater.*, 2023, **35**, 2203364.
376   18 H. Fang, S. Wu, T. Ayvali, J. Zheng, J. Fellowes, P.-L. Ho, K. C. Leung, A. Large, G. Held,
377      R. Kato, K. Suenaga, Y. I. A. Reyes, H. V. Thang, H.-Y. T. Chen and S. C. E. Tsang, *Nat.*

378      *Commun.*, 2023, **14**, 647.

379  19  J. Yu, Q. He, G. Yang, W. Zhou, Z. Shao and M. Ni, *ACS Catal.*, 2019, **9**, 9973–10011.

380  20  A. M. Abdel-Mageed, K. Wiese, M. Parlinska-Wojtan, J. Rabeah, A. Brückner and R. J.
381      Behm, *Appl. Catal. B Environ.*, 2020, **270**, 118846.

382  21  K. Qadir, S. M. Kim, H. Seo, B. S. Mun, F. A. Akgul, Z. Liu and J. Y. Park, *J. Phys. Chem. C*,
383      2013, **117**, 13108–13113.

384  22  K. Xu, X.-C. Hu, C. Ma, P. Wang, W.-W. Wang and C.-J. Jia, *Catal. Sci. Technol.*, 2023, **13**,
385      6254–6263.

386  23  J. Li, Z. Liu, D. A. Cullen, W. Hu, J. Huang, L. Yao, Z. Peng, P. Liao and R. Wang, *ACS*
387      *Catal.*, 2019, **9**, 11088–11103.

388  24  W. Li, H. Zhang, J. Wang, W. Qiao, L. Ling and D. Long, *Adv. Mater. Interfaces*, 2016, **3**,
389      1500711.

390  25  R. Arenal, A. C. Ferrari, S. Reich, L. Wirtz, J.-Y. Mevellec, S. Lefrant, A. Rubio and A.
391      Loiseau, *Nano Lett.*, 2006, **6**, 1812–1816.

392  26  D. Ugarte, A. Châtelain and W. A. De Heer, *Science*, 1996, **274**, 1897–1899.

393  27  X. Pan and X. Bao, *Acc. Chem. Res.*, 2011, **44**, 553–562.

394  28  Z. Peralta-Inga, P. Lane, J. S. Murray, S. Boyd, M. E. Grice, C. J. O'Connor and P. Politzer,
395      *Nano Lett.*, 2003, **3**, 21–28.

396  29  A. Celik-Aktas, J.-M. Zuo, J. F. Stubbins, C. Tang and Y. Bando, *Acta Crystallogr. A*, 2005,
397      **61**, 533–541.

398  30  D. J. Morgan, *Surf. Interface Anal.*, 2015, **47**, 1072–1079.

399  31  S. Carenco, C. Sassoye, M. Faustini, P. Eloy, D. P. Debecker, H. Bluhm and M. Salmeron, *J.*
400      *Phys. Chem. C*, 2016, **120**, 15354–15361.

401  32  S. López-Rodríguez, A. Davó-Quiñonero, E. Bailón-García, D. Lozano-Castelló and A.
402      Bueno-López, *Mol. Catal.*, 2021, **515**, 111911.

403  33  K. Qadir, S. H. Joo, B. S. Mun, D. R. Butcher, J. R. Renzas, F. Aksoy, Z. Liu, G. A. Somorjai
404      and J. Y. Park, *Nano Lett.*, 2012, **12**, 5761–5768.

405  34  S. M. Csicsery, *Zeolites*, 1984, **4**, 202–213.

406  35  I. Rossetti and L. Forni, *Appl. Catal. Gen.*, 2005, **282**, 315–320.

407  36  R. Klaewkla, M. Arend and W. F., in *Mass Transfer - Advanced Aspects*, ed. H. Nakajima,
408      InTech, 2011.

409  37  P. Serp, *Appl. Catal. Gen.*, 2003, **253**, 337–358.

410  38  M. J. Ledoux, R. Vieira, C. Pham-Huu and N. Keller, *J. Catal.*, 2003, **216**, 333–342.

411  39  J.-P. Tessonnier, L. Pesant, G. Ehret, M. J. Ledoux and C. Pham-Huu, *Appl. Catal. Gen.*,
412      2005, **288**, 203–210.

413  40  Z. Duan and G. Henkelman, *ACS Catal.*, 2014, **4**, 3435–3443.

414  41  J. Yang, S. Hu, Y. Fang, S. Hoang, L. Li, W. Yang, Z. Liang, J. Wu, J. Hu, W. Xiao, C. Pan,
415      Z. Luo, J. Ding, L. Zhang and Y. Guo, *ACS Catal.*, 2019, **9**, 9751–9763.

416  42  F. Li, Y. Li, X. C. Zeng and Z. Chen, *ACS Catal.*, 2015, **5**, 544–552.

417  43  C. H. F. Peden, D. W. Goodman, M. D. Weisel and F. M. Hoffmann, *Surf. Sci.*, 1991, **253**,
418      44–58.

419  44  C. Huang, X. Ye, C. Chen, S. Lin and D. Xie, *Comput. Theor. Chem.*, 2013, **1011**, 5–10.

420  45  M. J. Sharif, M. Kitano, Y. Inoue, Y. Niwa, H. Abe, T. Yokoyama, M. Hara and H. Hosono,
421      *J. Phys. Chem. C*, 2015, **119**, 11725–11731.

422  46  E. Gonzalez-A, R. Rangel, A. Solís-Garcia, A. M. Venezia and T. A. Zepeda, *Mol. Catal.*,
423      2020, **493**, 111086.

424  47 C. Fang, X. Jiang, J. Hu, J. Song, N. Sun, D. Zhang and L. Kuai, *ACS Appl. Mater. Interfaces*,
425      2021, **13**, 5079–5087.
426  48 B. Huang, H. Kobayashi, T. Yamamoto, S. Matsumura, Y. Nishida, K. Sato, K. Nagaoka, S.
427      Kawaguchi, Y. Kubota and H. Kitagawa, *J. Am. Chem. Soc.*, 2017, **139**, 4643–4646.
428  49 X. Liu, J. Zeng, J. Wang, W. Shi and T. Zhu, *Catal. Sci. Technol.*, 2016, **6**, 4337–4344.
429  50 J. Li, Z. Liu and R. Wang, *J. Colloid Interface Sci.*, 2018, **531**, 204–215.
430

September 12, 2024

## Data Availability Statement

The data that support the findings of the research are available on request from the corresponding author.

Sincerely,

Dr. Tae Jin Kim
Associate professor, Graduate Program Director
Materials Science and Chemical Engineering Dept.
Stony Brook University, Stony Brook, NY, 11794
Phone: 1-631-632-8433, Fax: 1-631-632-8052
E-mail: taejin.kim@stonybrook.edu